6

Isolators

An isolator is a one-input, one-output component that transmits light in a forward direction and blocks light in a reverse direction. All isolators incorporate at least one Faraday rotator (FR) as the nonreciprocal element. There are two classes of isolators: polarizing isolators that isolate by rejecting the unwanted polarization state, and polarization-independent isolators that isolate by spatial filtering. Polarizing isolators have a single optical path that transits a first polarizer, the FR, and a second polarizer. In the isolation direction the unwanted polarization is either absorbed or deflected. Polarization-independent isolators use polarization diversity to form two co-directional optical paths, one for each polarization. Along the forward direction the two paths recombine at the collimator while along the reverse direction the two paths fall outside of the fiber aperture.

Analysis of the polarizing isolator highlights the issues regarding transmission and isolation as a function of temperature, wavelength, and manufacturing error. The materials-related shortcomings of iron garnets are apparent in this analysis. The polarization-diversity schemes to realize polarization-independent isolators guide the best choice lensing system and open up the issue of path-length balancing. A path-length imbalance imparts polarization-mode dispersion (PMD). PMD-compensated isolators are realized by select changes in the optical elements used to build the isolator or by explicit addition of a compensating element.

6.1 Polarizing Isolator

Polarizing isolators were the first isolator type to demonstrate the importance of the nonreciprocal Faraday rotator. Early literature shows a Verdet-based isolator [28] and a terbium-aluminum garnet-based isolator [16]. A garnet-based polarizing isolator is illustrated in Fig. 6.1. The polarizing axes of the first and second polarizers are rotated 45° with respect to one another. A Faraday rotator with a fixed magnetization direction is placed between the

Jay N. Damask: Polarization Optics in Telecommunications, SSOS 101, 247–272 (2005)
© Springer-Verlag New York, Inc. 2005

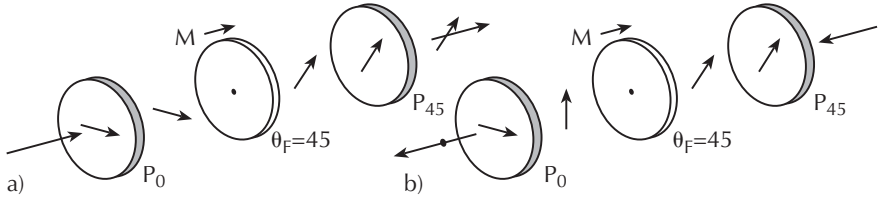


Fig. 6.1. Faraday rotation of 45° between two polarizers. Polarizer and analyzer are rotated 45° with respect to one another to maximize transmission and isolation. a) Forward path allows transmission. Horizontal linear polarization is rotated +45° by FR and transits analyzer $\mathcal{P}_{45}$ without loss. b) Reverse, isolation path. +45° linear polarization is rotated +45° by FR and is extinguished by analyzer $\mathcal{P}_o$.

two polarizers. In practice the FR is a saturated Bi:RIG iron garnet (cf. §4.2.3) where the magnetization is fixed by a permanent magnet, such as Sm-Co, or where the iron garnet is latching and pre-poled. Multi-magnet schemes have been proposed to concentrate the magnetic field around the FR [5, 6, 18], but in practice a single magnet is used. The FR is designed to rotate a linear polarization state by +45° (or −45°) irrespective of transit direction.

In the forward, or transmission, direction, the lead polarizer $\mathcal{P}_o$ polarizes the light along the horizontal (the absolute direction being, of course, immaterial). The FR subsequently rotates the polarization by +45°, which aligns it for complete transmission through the second polarizer $\mathcal{P}_{45}$. In the reverse, or isolation, direction, the lead polarizer $\mathcal{P}_{45}$ polarizes the light at +45°. The FR rotates the polarization by +45°, at which point the polarization is clipped by the second polarizer $\mathcal{P}_o$. The second polarizer absorbs the light.

Problems with this system arise from the wavelength and temperature dependence of the FR plate, manufacturing error of the plate length, residual linear birefringence in the garnet, and multiple reflections due to imperfect antireflection coatings. Residual linear birefringence is reduced by removing the garnet from its substrate and annealing the film, although linear birefringence remains the ultimate limiting factor. Imperfect antireflection coatings cause multiple reflections inside the material; each full pass rotates the polarization by approximately 90°, so every other round-trip reflection creates a polarization component that reduces isolation.

The specific rotation of an iron garnet has temperature and wavelength dependencies:

$$\theta'_F(\lambda, T) = \frac{2\pi}{\lambda}\,\Delta n(\lambda, T) \tag{6.1.1}$$

The Faraday rotation angle θ_F for a plate of length L is

$$\theta_F = \theta'_F L \tag{6.1.2}$$

At a nominal temperature, wavelength, and thickness the target rotation is θ_{Fo}. The actual rotation for small deviations is $\theta_F = \theta_{Fo} + \Delta\theta_F$, where the total deviation from the target is

$$\Delta\theta_F = \frac{d\theta_F}{dL}\,\Delta L + \frac{d\theta_F}{dT}\,\Delta T + \frac{d\theta_F}{d\lambda}\,\Delta\lambda \tag{6.1.3}$$

The first term comes from manufacturing error, the second from temperature dependence of the garnet, and the third from the total wavelength dependence. The wavelength dependence has two components, one from the fixed waveplate thickness and the other from wavelength-dependent Δn of the garnet:

$$\frac{d\theta_F}{d\lambda}\,\Delta\lambda = \frac{\Delta\omega}{\omega_o}\,\theta_{Fo} + \frac{1}{\Delta n}\left(\frac{d\Delta n}{d\lambda}\right)\theta_{Fo}\,\Delta\lambda \tag{6.1.4}$$

The first term is simply the frequency dependence of the waveplate and comes from (4.6.13) on page 182. The second term highlights the material dependence on wavelength. This term is not zero and generally increases the overall wavelength dependence of the plate.

Recall that the eigen-axis of a Faraday rotator is $\pm\hat{s}_3$. The associated Jones operator U_F is

$$U_F = \cos\theta_F I \mp j\sigma_3 \sin\theta_F \tag{6.1.5}$$

The operator U_F must be treated carefully: due to the nonreciprocal nature of the FR, the signs of θ_F and σ_3 are invariant to transit direction. The $\mp$ sign encompasses only the magnetization direction $\mathbf{M}$ and the particular Bi:RIG material. Once these are fixed, the sign is fixed. The point of including the $\mp$ sign is to represent the possibility that the FR or permanent magnet can be flipped around. Without loss of generality, the $(-)$ sign will be used in the following.

Also, recall that a polarizer is represented by the projection matrix (2.5.2) on page 52. The two polarizers for this nominal isolator are

$$\mathcal{P}_o = \begin{pmatrix} 1 & 0 \\ 0 & 0 \end{pmatrix}, \quad \text{and} \quad \mathcal{P}_{45} = \frac{1}{2}\begin{pmatrix} 1 & 1 \\ 1 & 1 \end{pmatrix} \tag{6.1.6}$$

Equipped with these polarizer and FR matrices, the forward and reverse isolator paths can be analyzed.

In the forward direction, output state $|t\rangle$ is generated from input state $|s\rangle$ via

$$|t\rangle = \mathcal{P}_{45} U_F \mathcal{P}_o\,|s\rangle$$

Recalling that $\mathcal{P}^2 = \mathcal{P}$, the output intensity is

$$\langle t\,|t\rangle = \langle s\,|\,{\mathcal{P}_o}^{\dagger}{U_F}^{\dagger}\mathcal{P}_{45}U_F\mathcal{P}_o\,|s\rangle \tag{6.1.7}$$

Combining (6.1.5-6.1.6) into (6.1.7) gives the forward transmission matrix

$$T_{\text{iso}}^{+} = \frac{1}{2}\left(1 + \sin 2\theta_F\right)\begin{pmatrix} 1 & 0 \\ 0 & 0 \end{pmatrix}$$

At the nominal Faraday rotation angle $\theta_{Fo} = +45^\circ$ the transmission is unity.

In the reverse direction, the output state $|s'\rangle$ is generated from input state $|t'\rangle$ via

$$|s'\rangle = \mathcal{P}_o U_F \mathcal{P}_{45} |t'\rangle$$

The output intensity is

$$\langle s' | s' \rangle = \langle t' | {\mathcal{P}_{45}}^\dagger {U_F}^\dagger \mathcal{P}_o U_F \mathcal{P}_{45} | t' \rangle$$

which yields the reverse transmission matrix

$$T_{\text{iso}}^- = \frac{1}{4}(1 - \sin 2\theta_F) \begin{pmatrix} 1 & 1 \\ 1 & 1 \end{pmatrix}$$

Stripping away the polarization orientation, the norm of T_{iso}^- gives the total reverse intensity

$$|T_{\text{iso}}^-| = \frac{1}{2}(1 - \sin 2\theta_F) \tag{6.1.8}$$

At the nominal Faraday rotation angle $\theta_{Fo} = +45°$ the transmission is zero.

The nominal forward and reverse transmissions are unity and zero, respectively. However, rotation deviations included in (6.1.3) degrade the performance. Accounting for deviations, the forward and reverse transmissions are

$$T_{\text{iso}}^+ = \cos^2 \Delta\theta_F, \quad \text{and} \quad T_{\text{iso}}^- = \sin^2 \Delta\theta_F$$

Isolation is defined as

$$I_{\text{iso}} = -10 \times \log_{10}\left(T_{\text{iso}}^-\right) \quad \text{(dB)} \tag{6.1.9}$$

The forward transmission, or insertion loss (IL), changes to second order with change in $\Delta\theta_F$ and the isolation changes to first order.

Consider the frequency dependence of the rotation alone:

$$\Delta\theta_F = \frac{\omega - \omega_o}{\omega_o}\, \theta_{Fo} \tag{6.1.10}$$

where θ_{Fo} coincides with frequency ω_o. Figure 6.2(a) plots the isolation as a function of frequency over the C-band. This idealized FR imparts +45° rotation at 194.1 THz. Recalling the spectral coverage for the C-band from (4.1.5) on page 146, the frequency deviation from center is $\Delta f/f_o = \pm 1.03\%$, which translates to $\Delta\theta_F \simeq \pm 0.45°$. In turn, the minimum isolation on either side of the C-band is $I_{\text{iso}} \simeq 42$ dB. This is a high level of isolation that under ideal conditions would be suitable for many applications.

The remaining three factors further degrade the practical performance of an isolator. One factor is that the FR plate is generally toleranced to $\theta_F = 45 \pm 1°$ [17]. This translates into a frequency shift of the maximum isolation point. Figure 6.2(b) shows such an frequency shift for $\Delta\theta_F = -0.25°$. The isolation for a 1° rotation error, combined with the 0.45° frequency-dependent

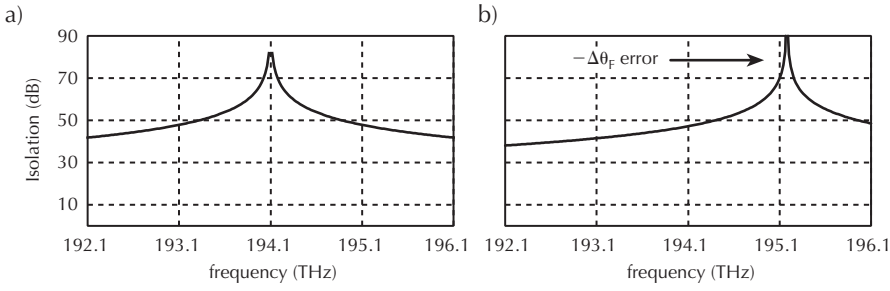


Fig. 6.2. The frequency dependence of the Faraday rotation plate, ignoring material wavelength dependence, results in frequency-dependent isolation. a) Isolation over the C-band. b) Any change in the FR angle changes the frequency of peak isolation.

rotation, gives $\Delta\theta_F = 1.45°$, or $I_{\rm iso} \simeq 32$ dB. This level of isolation is commonly found in component specification sheets of polarization-independent isolators at room temperature [9].

The remaining two factors are the change in specific rotation as a function of temperature and wavelength. Examples of practical temperature and wavelength ranges are 0°C to +70°C and the short to long wavelength sides of the C-band. Taking room temperature as RT = 25°C, the maximum temperature excursion is $\Delta T = 45°$C. The C-band is covered by $\Delta\lambda = \pm 16$ nm.

The total of all four deviation factors should not cause worst-case isolation to fall below a specified value. For example, $I_{\rm iso} = 20$ dB requires $\Delta\theta_F|_{\rm max} = \pm 5.75°$. Subtracting 1.0° for manufacturing tolerance, there remains 4.75° for temperature and total wavelength dependencies. Setting the coefficients equal gives

$$\frac{d\theta_F}{d\lambda} \simeq 0.08°/\text{nm}, \quad \text{and} \quad \frac{d\theta_F}{dT} \simeq 0.08°/°\text{C} \tag{6.1.11}$$

These coefficients translate to a 1.3° allowance for total wavelength dependence and a 3.6° allowance for temperature dependence. Moreover, the wavelength-dependent component of the waveplate is 0.45°, so the material component must be less than 0.85°. As discussed in §4.2.3, these coefficients are challenging from a materials standpoint.

That the worst-case isolation can fall to 20 dB even with perfect polarizing elements is quite a remarkable fact. The relatively poor performance of the FR over the full operating range necessitates two-stage isolators for high-performance applications.

One simple improvement ubiquitous in the industry is to change the angle between polarizers to account for manufacturing error of the FR plate. A 1° manufacturing error in rotation is 18% of the total error budget. In the isolation direction, a manufacturing error of $\Delta\theta_F$ is made up with a one-to-one change in the rotation of the analyzing polarizer. This, however, changes the insertion loss of the forward direction. If the analyzer is rotated by angle 45°

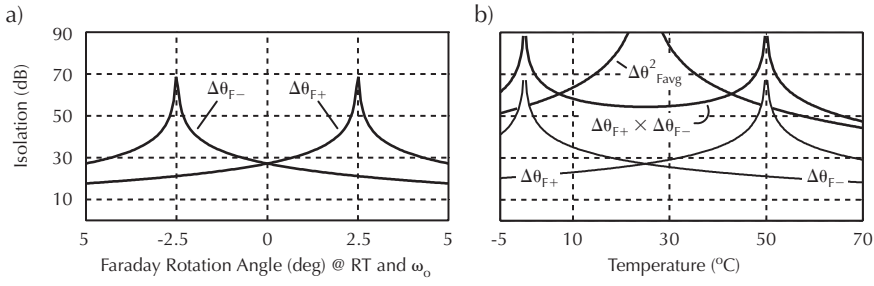


Fig. 6.3. Two-stage, complementary FR configuration [19]. a) One stage has FR biased to an angle below 45° while the other stage is biased above 45°. b) Two-stage isolation across temperature. The product of positive- and negative-biased FR angles provides better overall isolation than two stages with the same FR centered at 25°C.

$+\rho$, the insertion loss varies with analyzer error ρ as

$$|T^+_{\text{iso}}(\rho)| = \cos^2 2\rho \tag{6.1.12}$$

Note that the IL goes as 2ρ, but still imparts only a second-order change.

To improve the overall isolation, a two-stage isolator is necessary. Shiraishi proposes a two-stage isolator where the two FRs are detuned in frequency about a center frequency [19, 20]. The detuning is easily achieved by polishing the iron garnets to different thicknesses. For detuning rotations $\Delta\theta_{F1}$ and $\Delta\theta_{F2}$, the forward and reverse transmissions in cascade are

$$T^+_{\text{iso}} = \cos^2 \Delta\theta_{F1} \cos^2 \Delta\theta_{F2} \tag{6.1.13a}$$

$$T^-_{\text{iso}} = \sin^2 \Delta\theta_{F1} \sin^2 \Delta\theta_{F2} \tag{6.1.13b}$$

As the peak isolation frequencies shift with wavelength and temperature, the overall isolation remains higher than a two-stage isolator using the same FR. Figure 6.3 illustrates the principle. Figure 6.3(a) plots the frequency-dependent isolation from two individual isolators where the FRs are different. The combined isolation over temperature is shown in Fig. 6.3(b). The combined isolation does not fall below 48 dB while that for two stages of a single FR type centered at 25°C is slightly worst at both temperature extremes.

6.2 Comparison of Lens Systems

The next logical step in isolator development is the polarization-independent (PI) isolator. The are two different types of PI isolators: deflection-type and displacement-type. These types are detailed in the following sections. Here, a look at the different optimal lensing systems serves to emphasize the contrast between the two isolator types.

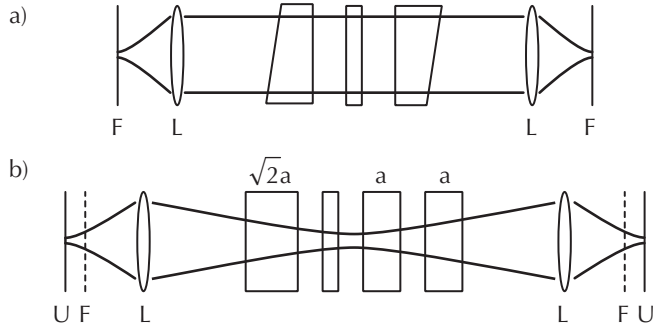


Fig. 6.4. Lensing systems for deflection and displacement isolators. a) Deflection isolator uses a collimating design for shortest length. A collimating lens system transforms angle in image space to position on the focal plane. b) Displacement isolator uses a focusing design to minimize the necessary walkoff, in turn minimizing the length of the birefringent crystals.

Figure 6.4 illustrates a deflection-type isolator (top) and displacement-type isolator (bottom) and their respective collimating and focusing lens systems (cf. §5.4). The core of the deflection isolator changes the angle of the beam as a function of propagation direction. The collimating system transforms angle into lateral offset at the focal plane, which leads to spatial filtering in the isolation direction. The core of the displacement isolator operates on the principle of walkoff, where beams are laterally displaced but remain collinear. The lensing system transforms offset in the image plane to offset in the object plane, the magnification of the system being the scale factor between the two offsets. These offsets also lead to spatial filtering in the isolation direction.

Figure 6.5 illustrates the different configurations relevant to isolator designs. Figure 6.5(a) shows an idealized alignment between the axis of a collimated beam and a lens. All rays converge at the focal plane F. Figure 6.5(b) shows the same collimating lens but where the beam is offset from the lens axis by y_o, the angle remaining aligned to that axis. Since angle transforms to offset for a collimating system, all rays converge at the original focal point of Fig. 6.5(a), albeit along the inclination θ_c. Figure 6.5(c) shows a collimated beam deflected by angle θ_d; the beam is focused to point y_i, which is offset from the on-axis focal point. The focusing lens shown in Fig. 6.5(d) shows a diverging beam offset from and parallel to the lens axis. On the object plane U the rays focus to a point offset by y_i. If the magnification of the system is M, the spot size w_o and offset y_o on the object plane are scaled to $w_i = w_o/M$ and $y_i = y_o/M$ on the image plane.

With these two configurations in mind, the action of the deflection-type and displacement-type isolator cores and their relationship to the lensing systems will be more apparent.

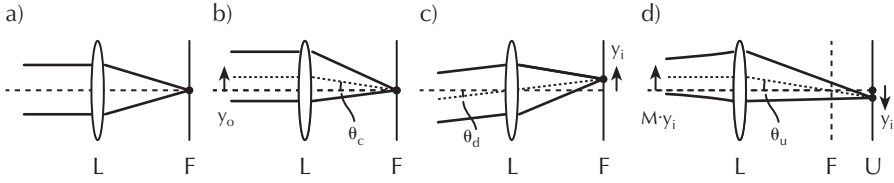


Fig. 6.5. Isolator-related beam transformations through a lens. Collimated systems are in (a–c) and a focusing system is in (d). a) Collimated beam travels through center of lens. b) Offset collimated beam focuses on same spot as (a). c) Deflected beam translates to focal-point offset. d) Offset diverging beam is imaged to a point offset from center.

6.3 Deflection-Type Isolators

The first polarization-independent isolators are reported in [12, 13] and [26]. These isolators used iron garnet Faraday rotators and polarization diversity schemes. However, the number of parts and required size of the isolators, much less the deleterious inclusion of a bandwidth-limiting half-wave waveplate in the design by [12], makes these PI isolators impractical.

The first practical polarization-independent isolator was invented by Shirasaki [21, 22]. The Shirasaki isolator is a deflection-type isolator that uses birefringent wedges to create polarization diversity and to polarize and analyze the light. The core of the deflection isolator is illustrated in Fig. 6.6. Two birefringent wedge prisms (cf. §4.7) are oriented as shown and a Faraday rotator is placed in between. The wedge angle of the prism deflects the incoming light, and the birefringence of the prism creates a polarization-dependent deflection. The extraordinary axis of the birefringent crystal is cut to lie in the face of the prism; in this way there is no walkoff but there is polarization-dependent refraction. The only required relation between the extraordinary axes of the two wedges is that they are $\pm 45°$ apart in the plane perpendicular to propagation. As illustrated in Fig. 6.6(a), when the wedge is cut such that the e-axis is at $+22.5°$ from an edge of the rectangular aperture, the same wedge can be used at both ends. The Faraday rotator is a Bi:RIG iron garnet that has its saturated magnetization maintained by a permanent magnet, Fig. 6.6(b). Originally, a YIG garnet was used.

The forward and reverse ray-trace diagrams are shown in Fig. 6.7. (A detailed ray-trace that includes chief and marginal rays is available in [1]). In the forward direction (Fig. 6.7(a)), the input light is refracted by the first wedge into u- and v-paths, the paths being orthogonally polarized. On plane (a) the point and polarization of the u- and v-paths are indicated, where the polarization of the v-path is extraordinary in relation to the first wedge while the u-path is ordinary. Transit of the two beams through the FR rotates their linear polarization states by 45° in a clockwise manner. The polarizations of these beams are now aligned to the extraordinary axis of the second wedge. The v-path refracts based on the extraordinary index of the second wedge

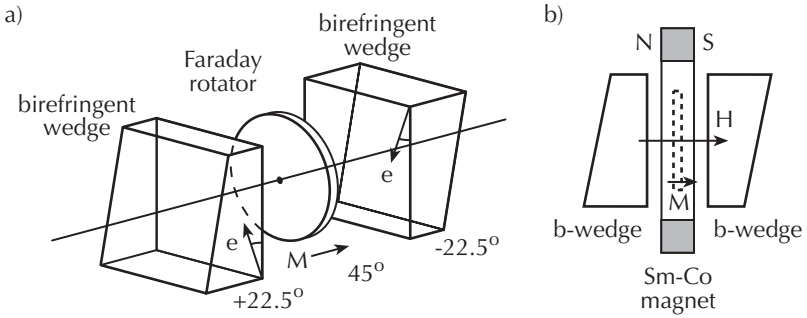


Fig. 6.6. Core of single-stage deflection-type isolator. a) Two birefringent wedges having the same wedge angle are configured as shown. A Faraday rotator plate is located between the wedges and the magnetization vector points along the optic axis. b) The magnetization of the FR is typically held in saturation by a permanent magnet such as Sm-Co.

while the u-path refracts based on the ordinary index. Provided wedge angles and materials are the same, the second wedge deflection cancels the first. The u- and v-paths run collinear before the second lens, the lens brings the two beams to focus at the same point.

In the reverse direction the two wedges conspire to deflect the beams out of the aperture of the return fiber. Accounting for the polarization rotation from the Faraday rotator, the two wedges form a Wollaston prism as viewed from the isolation direction. As shown in Fig. 6.7(b), the wedge w_2 imparts double refraction based on the polarization state of the input light (the same as wedge w_1 for the forward path). The linear polarization states of paths u' and v' are shown at plane (a′). Transit through the FR again rotates the linear polarization states by 45° in a clockwise manner. At the leading face of wedge w_1 the polarizations on the two paths are not aligned to the wedge. The v'-path which was refracted by the extraordinary index in wedge w_2 now refracts by the ordinary index, retaining a residual deflection that is calculated below. The opposite alignment occurs for the u'-path with the effect of a residual deflection in the opposite direction. Together, the two wedges split and deflect the incoming light.

There are four calculations required for the deflection-type isolator: in the forward direction, the loss due to the beam offset before lens L_2; in the reverse direction, the loss due to the beam deflection by the wedge pair; the angle of the wedge; and the path-length imbalance, or PMD, in the forward direction.

In the forward direction, offset y_o on the left side of lens L_2 is mapped by the lens into tilt angle θ_c. For simplicity consider that the overall magnification of the lens pair is unity. The beam waists w_o of the fiber and focused-beam modes are then the same. Using (5.4.11) on page 243, the mode-overlap due to tilt θ_c is

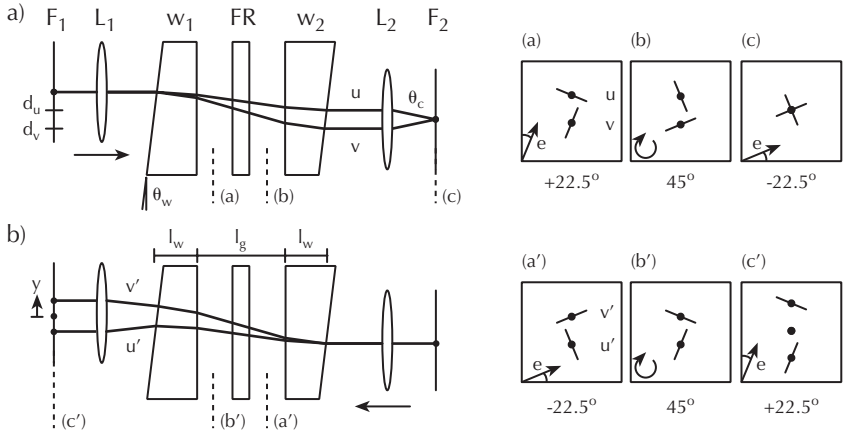


Fig. 6.7. Ray-trace diagrams for forward and isolation directions in a deflection-type isolator. a) Forward-path ray trace: beams of cross polarizations converge at the output fiber. Right: spot diagram through core. b) Isolation-path ray trace: beams of cross polarizations are deflected by the wedges, falling outside of the aperture of the return fiber. The frames around the spot diagrams are a guide for the eye only.

$$\mathcal{I}_b = \exp\left(-\frac{\theta_c^2 k^2 w_o^2}{4}\right) \tag{6.3.1}$$

where k is the wavenumber and the tilt angle θ_c is related to offset y_o and lens focal length f via

$$y_o = \theta_c f \tag{6.3.2}$$

The beam offset is therefore related to the lens parameters and mode overlap as

$$y_o = \frac{2f}{kw_o}\sqrt{-\ln \mathcal{I}_b} \tag{6.3.3}$$

The offset in turn is determined by the difference in displacement between the u and v paths. The displacement difference is

$$d_v - d_u = (n_e - n_o)\,\theta_w \left(\frac{2l_w}{n_e n_o} + l_g\right) \tag{6.3.4}$$

where θ_w is the angle of the wedge, l_w and l_g are the wedge and gap lengths, and n_e and n_o are the extraordinary and ordinary refractive indices. (Note that if the wedge prisms were exchanged such that the flat facets face the lenses, only the gap length l_g would contribute to the displacement.) Provided that the axis of lens L_2 bisects the displacements d_u and d_v, the offset is related to the displacement difference as $y_o = (d_v - d_u)/2$.

To appreciate the order of magnitude for tolerable offset y_o, consider $f = 1$ mm, $\omega = 2\pi \times 194.1$ THz, and $w_o = 5$ μm. For an insertion loss of $\mathcal{I}_b = -0.05$ dB attributable to the beam displacement (and not imperfect AR coatings or material losses), the required offset is $y_o \simeq 7$ μm.

In the reverse direction, deflection θ_d imparted by the wedge pair is mapped by lens L_1 to an offset position y_i on focal plane F_1. Displacement of the reverse beams from lens center also creates a tilt angle when mapped through the lens, but given the small displacement calculated for the forward direction this angle is ignored here. Provided unity magnification, the mode-overlap due to displacement y_i between the focused beams and the fiber facet, given by (5.4.8) on page 242, is

$$\mathcal{I}_a = \exp\left(-\frac{y_i^2}{4w_o^2}\right) \tag{6.3.5}$$

where the displacement y_i is related to the deflection angle via

$$y_i = \theta_d f \tag{6.3.6}$$

The required deflection angle for a given isolation $\mathcal{I}_a$ is therefore

$$\theta_d = \frac{2w_o}{f}\sqrt{-\ln \mathcal{I}_a} \tag{6.3.7}$$

Continuing with the same example, an isolation of $I_{\text{iso}} = -45$ dB requires a deflection angle of $\theta_d \simeq 1.8°$.

The deflection angle θ_d is directly related to the wedge angle θ_w and the birefringence of the crystal. Recall the deflection angle β for a small-angle prism, given by (4.7.2) on page 199. Consider first the forward u-path. The deflections due to wedges w_1 and w_2 are

$$\beta_{u1} = -(n_o - 1)\theta_w \tag{6.3.8a}$$

$$\beta_{u2} = (n_o - 1)\theta_w \tag{6.3.8b}$$

Both deflections are based on the ordinary refractive index seen by the u path. One sign is the opposite of the other because the based of the wedge prisms are inverted. The total deflection is $\beta_{u1} + \beta_{u2} = 0$. This is consistent with the previous analysis of the forward path.

In the reverse direction the wedge deflections do not cancel. Following the same analysis, the deflections of the u'-path are

$$\beta_{u'2} = (n_o - 1)\theta_w \tag{6.3.9a}$$

$$\beta_{u'1} = -(n_e - 1)\theta_w \tag{6.3.9b}$$

The total deflection of the u'-path is therefore

$$\beta_{u'} = \theta_d = -(n_e - n_o)\theta_w \tag{6.3.10}$$

The deflection along the v'-path is the negative of (6.3.10).

The deflection angle θ_d can now be associated with the isolation requirement. Substitution of (6.3.10) into (6.3.7) gives

$$\theta_w = \frac{2w_o}{\Delta n f}\sqrt{-\ln \mathcal{I}_a} \tag{6.3.11}$$

Using the exemplar values from above and using YVO_4 as the wedge material, the wedge angle to provide $I_{\rm iso} = -45$ dB is $\theta_w \simeq 9.0°$. This angle is consistent with YVO_4 wedges that are used in the industry.

Together, equations (6.3.3), (6.3.4), and (6.3.11) define the specification of a wedge-type isolator. For these three equations there are three free variables: focal length f, wedge thickness l_w, and gap length l_g. The remaining parameters are the fiber, the material, and the transmission and isolation specifications.

Table 6.1 presents deflection-type isolator specifications for a one-stage isolator reported by a manufacturer. The high return loss is achieved by collimator selection as well as orienting the angled facet of the wedges toward the collimators to minimize back reflection. Power handling is limited by the collimator technology (cf. §5.1), and as reported here, the collimators are likely air-gap type.

The remaining calculation is the path imbalance, commonly referred to as the PMD of the device. Here, the use of the term PMD is not precise, and while the industry will not likely change its terminology based on a small discrepancy, the discerning reader should know the difference. In the forward direction the u- and v-paths experience different refractive indices. Accordingly, one path is "fast" while the other is "slow." Since the paths are split according to polarization, one polarization state is delayed with respect to the other. This is, precisely, differential-group delay (DGD). Polarization-mode dispersion results from the concatenation of multiple, non-aligned DGD elements and is characterized in most cases by a PMD vector that changes its pointing direction with frequency. This is not the case for a single isolator. In this work, the PMD of a component will be used when relating to industry usage; but otherwise DGD, or τ, is used. For the deflection-type isolator, note that in the forward direction the u experiences the ordinary index, while the v experiences the extraordinary. This is true through both crystals. The FR does not impart any significant differential delay. Since the deflection angle differences are small for a practical isolator, the wedge length l_w approximates the actual path. The differential-group delay τ between the two paths is

$$\tau \simeq \frac{2(n_{\rm g,e} - n_{\rm g,o})l_w}{c} \tag{6.3.12}$$

where $n_{\rm g,e}$ and $n_{\rm g,o}$ are the group indices of the e- and o-axes. A YVO_4 wedge 0.5 mm long at the base with a 9° wedge has a path length of approximately 0.35 mm on the thin side. The differential-group delay for an isolator made from this deflection-type component is $\tau \simeq 0.45$ ps (cf. §4.2.2). Substitution of $LiNbO_3$ for YVO_4 can further reduce the differential-group delay at the expense of an increase in gap length and wedge angle. For example, $LiNbO_3$ wedges of the same length yields a differential-group delay of $\tau \simeq 0.16$ ps.

Table 6.1. Deflection-Type Isolator Technology Comparison

Specification[(a)]	**1-Stage**	**2-Stage**	**PMD-Comp**	**Units**
Isolation ($\lambda_c \pm 15$ nm, 23°C, all SOP)	32	60	32	dB
Isolation ($\lambda_c \pm 15$ nm, 0-70°C, all SOP)	22	42	22	dB
Insertion Loss (λ_c, 23°C, all SOP)	0.2	0.4	0.3	dB
Insertion Loss (λ_c, 0-70°C, all SOP)	0.3	0.6	0.5	dB
PMD	0.20	0.05	0.02	ps
PDL (λ_c, 23°C)		0.05		dB
Return loss (λ_c, 23°C)		60		dB
Power handling		1,000		mW
Operating temperature		0-70		°C

[(a)]Specification values reported by Koncent for C-band operation [9].

As a concluding remark, the deflection-type isolator can be generalized to a 2×2 port component to reduce size while increasing functionality [23].

6.4 Displacement-Type Isolators

Building on the spatial-walkoff method of polarization diversity first proposed in [12], Chang and Sorin developed a practical alternative to the Shirasaki isolator [2]. The Chang and Sorin isolator, herein called a displacement-type isolator, uses three birefringent walkoff crystals cut as parallelepiped blocks to achieve polarization independence. One of several variations of their isolator core is illustrated in Fig. 6.8 and its relation to the associated lensing system is found in Fig. 6.4(b).

The core is characterized by two walkoff blocks of length a and the remaining block of length $\sqrt{2}a$ placed in the sequence $\sqrt{2} : 1 : 1$. The Faraday rotator is located between the longer block and the first shorter block. All blocks are cut so as to impart beam walkoff between orthogonal linear polarization states (cf. §3.6.1). Accordingly, the extraordinary axis has vector components that lie both transverse and longitudinal to the optical path. To maximize that walkoff angle, the extraordinary axis is inclined into the crystal by about 45°; the precise optimal angle, being material dependent, is calculated from (3.6.24) on page 117. For example, the optimal angle of inclination from the optical axis for YVO_4 and rutile are both $\alpha_{\max} \simeq 47.8°$. The three walkoff crystals are cut so that the walkoff directions are different from one another. Following Fig. 6.8, the walkoff directions are $+90°$, $-45°$, and $+45°$ from front to back, respectively.

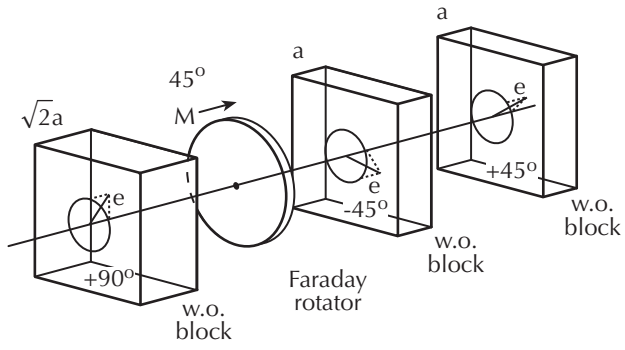


Fig. 6.8. Core of single-stage displacement-type isolator. a) Three birefringent walkoff blocks are configured as shown. The first block is $\sqrt{2}$ times longer than the other blocks. A Faraday rotator plate is located between first and second blocks. The cut of the extraordinary axes all maximize the walkoff and are oriented relative to one another as 90°, −45°, and −45°. The FR magnetization is typically held in saturation by a permanent magnet.

The principle of the displacement-type isolator differs from the deflection type. Within the displacement-type core, all beam paths run collinear between crystals. Within the crystals, polarizations are split and laterally shifted from one position to another. The interaction of the core with the lenses also differs because both offset and tilt are the principal means of spatial filtering. In order to minimize the crystal lengths, and corresponding spot-offset distances, a focusing lens system is used. The spatial distribution of spots in the transverse ray-trace diagram in the image plane (located within the core) is imaged onto the object plane (at the fiber face) by the receiving lens with a magnification factor M^{-1}. Only spots that fall within the fiber aperture are coupled, the remaining spots and associated beam paths are lost.

The forward and reverse ray-trace and spot diagrams are illustrated in Fig. 6.9. In the forward direction, walkoff block wo_1 splits the two polarizations and translates the extraordinary polarized light along the v-path to the top line. The FR rotates both u- and v-path polarization states by +45°. Walkoff block wo_2 translates the v-spot to the point indicated in frame (d) of Fig. 6.9(a). Lastly, walkoff block wo_3 translates the u-spot to overlap with the v-spot. Running collinear and along the L_2 lens axis, the combined forward beam is coupled into the output fiber.

In the reverse direction, the ray-trace through blocks wo_2 and wo_3 is the same as along the forward path. After the FR, however, the beams diverge. The Faraday rotator imparts a +45° rotation to the u'- and v'-path polarization states, creating a misalignment to the extraordinary axis of block wo_1. The misalignment causes the v'-path to trace a straight line through last block and the u'-path to walkoff in a downward direction. The resultant spot dia-

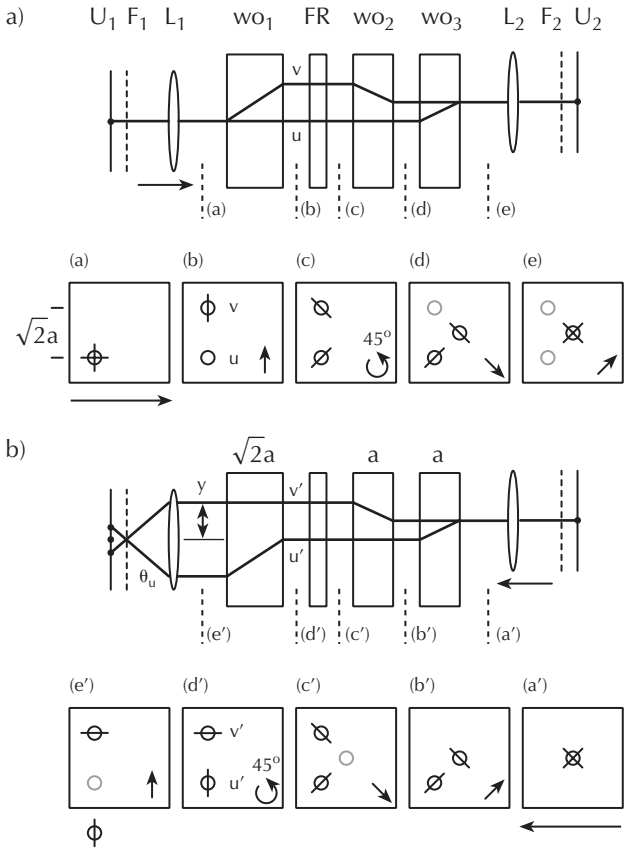


Fig. 6.9. Ray-trace and spot-trace diagrams for forward and isolation directions. a) Forward path splits polarizations along paths u- and v-paths. These beams, always collinear between blocks, converge at the output lens. b) Isolation path prevents beam convergence at the return lens and instead displaces both beams out of the aperture of the return fiber.

gram before lens L_1 is shown in frame (e′) of Fig. 6.9(b). With proper design the u'- and v'-spots fall outside of the fiber face and are lost.

There are several interlocking calculations required for the displacement-type isolator. In the forward direction the fiber-to-fiber coupling must have maximum transmission. While the fiber-to-fiber magnification is unity the single-lens magnification sets the Rayleigh length, which in turn should be on the same order as the lens-to-lens gap. In the reverse direction the requisite isolation determines, in conjunction with the lens magnification, the necessary spot offset. The spot offset in turn determines the unit crystal length a. Finally, the path-length imbalance, or DGD, is calculated for the forward direction.

In the forward direction, the depth-of-focus $2b$ should be on the same order as the lens-to-lens gap $L_{\rm gap}$ to ensure good coupling. In view of the focusing diagram in Fig. 5.16(b), the gaussian beam waist w_b between the lenses is related to the lens magnification and fiber beam waist as $w_b = Mw_o$. Using the expression for the confocal parameter (5.2.10) on page 222, the magnification is

$$M = \frac{1}{w_o}\sqrt{\frac{2b}{k_o}} \tag{6.4.1}$$

Note that the wavenumber k_o here is for free space.

In the reverse direction the requisite isolation along with the lens attributes determine the necessary spot offset. Referring to Fig. 6.9(b), the offset in frame (e′) maps to beam offset and tilt at the object plane U_1. The tilt angle θ_u is related to the offset via the focal length:

$$\theta_u = \frac{y_o}{f} \tag{6.4.2}$$

Moreover, the offset y_o to the right of the lens relates to the offset y_i on the U_1 plane through the magnification

$$y_o = My_i \tag{6.4.3}$$

Folding these relations into the overlap integral (5.4.10) on page 243, the offset is related to the isolation, lens, and fiber parameters via

$$y_o = \frac{2w_oM}{\sqrt{1+\left(\frac{k_o n w_o^2 M}{f}\right)^2}}\sqrt{-\ln \mathcal{I}_b} \tag{6.4.4}$$

As the mode overlap occurs within the fiber glass, the wavenumber k_o in (6.4.4) is scaled by the fiber index n. Finally, the u'- and v'-spot offsets from the axis of lens L_1 are both

$$y_o = \sqrt{2}a\gamma \tag{6.4.5}$$

where the walkoff angle γ is determined in general from (3.6.15) on page 110, or from (3.6.25) on page 117 for maximum walkoff. For example, the maximum walkoff in a YVO_4 crystal is $\gamma_{\rm max} \simeq 5.70°$.

Together, equations (6.4.1), (6.4.4), and (6.4.5) determine the crystal thickness a. For example, consider an approximate solution using YVO_4 where $I_{\rm iso} = -45$ dB, $2b = 5$ mm, $f = 1$ mm, $n = 1.44$ (of the fiber), and $\omega = 2\pi \times 194.1$ THz. The requisite magnification is $M \simeq 7.0$ mm. This in turn sets the necessary spot offset to $y_o \simeq 156$ μm. For this magnification, the minimum beam waist between the lenses is $2w_b \simeq 70$ μm and the displacement by the walkoff crystals is $y_o \simeq 2.2 \times (2w_b)$. Finally, the unit block length given the above walkoff angle is $a \simeq 1.1$ mm. As a check, the total length of the blocks is $(2+\sqrt{2})a \simeq 3.8$ mm, which is a bit less than the depth-of-focus.

The remaining calculation is the path imbalance in the forward direction. It should be clear that the differential-group delay through walkoff blocks wo_2 and wo_3 cancel. The imbalance is solely due to walkoff block wo_1. Within this block, the u-path sees the ordinary group index $n_{\text{g,o}}$, while the v-path sees the effective group index. The effective refractive index is a mixture of the ordinary and extraordinary refractive indices, the mixture set by the inclination angle α of the extraordinary from the optic axis, see (3.6.26) on page 117. The differential-group delay requires the effective group index, which generally is approximately the same as the refractive index for high birefringent crystals in the near infrared. Nonetheless, keeping track of the proper indices, the differential-group delay τ is

$$\tau = \frac{\sqrt{2}a\,(n_{\text{g}-\text{eff,e}} - n_{\text{g,o}})}{c} \tag{6.4.6}$$

Continuing with the example and using an effective refractive index, use of YVO_4 walkoff crystals imparts a differential-delay of $\tau \simeq 1.1$ ps. There is, in fact, a simple alternation that eliminates τ for a two-stage block-type isolator. This is detailed in §6.6.

As a concluding remark, folded architectures of the one-stage block-type isolator have been proposed wherein a single relay lens with a mirror backing is placed at a midpoint along the polarization evolution [4, 8, 15]. These isolators can be very compact, but none of the reports demonstrates an epoxy-free path.

6.5 Two-Stage Isolators

To increase the isolation over a wide temperature and wavelength range, two or more isolation stages are necessary. Two-stage isolators were already considered in §6.1 with respect to the garnet design. However, that discussion did not include polarization diversity. Nonetheless, the lessons from that earlier section apply here just as well.

Both the deflection-type and displacement-type isolators are expandable to two stages. Rather than blindly cascade two like stages, however, economies can be found to improve the performance or reduce the size of a two-stage component.

An example of a two-stage deflection-type isolator is illustrated in Fig. 6.10. Here the extraordinary axes of second wedge pair are rotated by 90° with respect to the first wedge pair. As indicated in the ray-trace diagram, this rotation leads to a convergence of the u- and v-paths in the forward direction. This is an improvement in PDL and alignment sensitivity over the single-stage deflection-type isolator. Moreover, the path imbalance along the forward path is cancelled. That is, the expected differential-group delay through the component is zero, although in practice differences in where the light paths intersect the the wedges leaves a residual imbalance. Table 6.1 shows the reported reduction in PMD value for a two-stage deflection-type isolator.

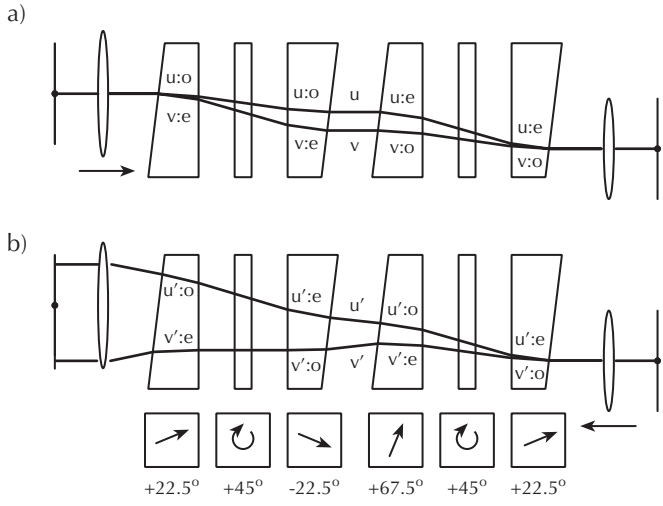


Fig. 6.10. A two-stage deflection-type isolator, one particular realization. To recombine the forward beams and to balance the u- and v-path lengths, the extraordinary axes of the second stage wedges are cut 90° in rotation from the first stage. a) Forward direction ray-trace. b) Isolation direction ray-trace. The deflection angles are twice that of the single-stage counterpart.

In the reverse direction, the u'- and v'-beams are deflected twice. The total deflection for either beam is therefore

$$\theta_d = \pm 2\,(n_e - n_o)\,\theta_w \tag{6.5.1}$$

Since the mode coupling goes exponentially with tilt angle, some redesign from a one-stage deflection may be possible to reduce the wedge angle.

A two-stage displacement-type isolator, in the configuration proposed by Chang and Sorin [3], is illustrated in Fig. 6.11. The $\sqrt{2}a$ block is placed between the two a blocks instead of in front. All three extraordinary axes are cut to maximize the walkoff, as before. Two FRs having the same rotary direction are added as indicated, and the walkoff direction in the plane perpendicular to the optic axis changes by 45° from one block to the next. Unlike the two-stage deflection-type isolator, this isolator does not increase the spatial filtering of the principal rays. However, the isolation is increased because light is scattered into more locations. Also, the differential-group delay is reduced, but not eliminated. Figure 6.11(a,b) details the principal and "error" paths along the forward and reverse directions, while (c) shows a detailed spot-evolution diagram. The error-paths originate from incorrect Faraday rotation. The differential-group delay for this two-stage isolator is

$$\tau = \frac{(\sqrt{2}-1)a\Delta n_{\mathrm{g}}}{c} \tag{6.5.2}$$

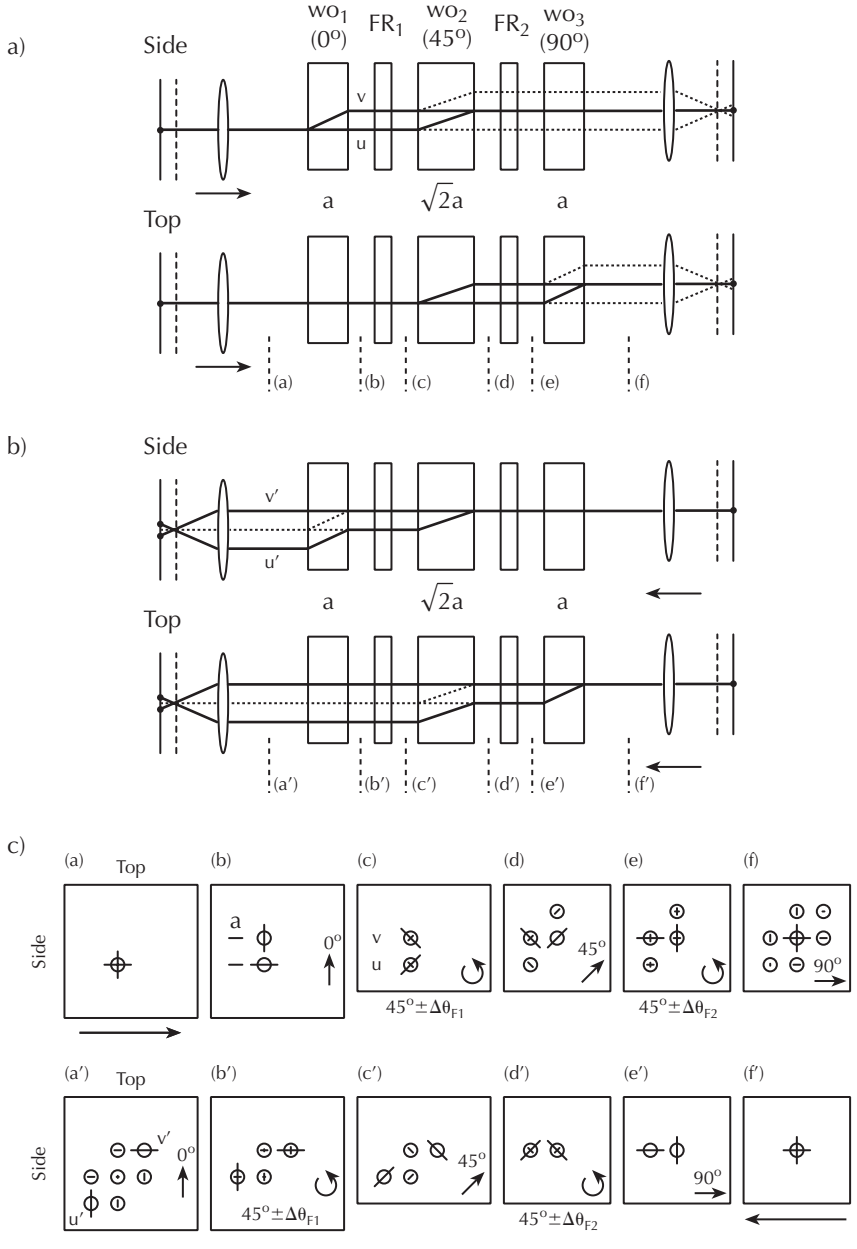


Fig. 6.11. Ray-trace and spot-trace diagrams for forward and isolation directions. This two-stage displacement isolator places walkoff blocks in a $1 : \sqrt{2} : 1$ sequence, with FRs located between blocks. Solid lines are nominal beam paths; dashed lines are error paths that occur when the Faraday rotation is not precisely 45°. a) Side and top views of forward paths. b) Side and top views of isolation paths. c) Spot-trace diagrams that include residual light from imperfect Faraday rotation.

where, as shown in the figure, the u-path somewhat cancels the differential-group delay from the v-path.

6.6 PMD-Compensated Isolators

The two-stage deflection-type isolator (Fig. 6.10) illustrated one way to compensate for the differential-group delay, colloquially known as PMD, in that configuration. There are other signification PMD-compensation techniques for one-stage isolators, both for deflection and displacement types.

For a one-stage deflection-type isolator, two methods have been invented to compensate for differential-group delay and differential beam displacement. Swan proposes the addition of a rhombohedral crystal with its extraordinary axis cut in the plane perpendicular to the optical path [24, 25] (Fig. 6.12(a)). The rhombohedral angle is set to combine the u- and v-paths through differential refraction. Alternatively, Xie proposes the addition of a parallelepiped crystal with its extraordinary axis cut as a walkoff block [7], Fig. 6.12(b). The parallelepiped length and extraordinary axis compensation angle are set concurrently to eliminate the DGD and differential beam displacement. There is some advantage of the Swan method over the Xie method because the former scheme lets the two wedge prisms be the same part where the latter method is best suited for two different prism parts.

Figure 6.12(a) shows the orientation of the three birefringent crystals in the Swan scheme. As in §6.3 the extraordinary axis of each wedge is cut at 22.5°. The orientation of the second wedge with respect to the first, as shown in the figure, automatically positions the second e-axis at 45° with respect to the first. In the forward path, the v-path refracts more than the u, assuming the wedges are made of positive uniaxial crystal. Concomitant with the greater refraction is an arrival-time delay of the v-path with respect to the u-path. In the forward direction the FR ensures that the v-path sees the e-axis of both wedges. Therefore, the ignoring the second-order correction for the refraction angle, DGD is accrued over length $2l_w$.

Accordingly, the rhombohedral compensation crystal is cut as a waveplate with its e-axis rotated 90° to the e-axis of the second wedge. That is, the extraordinary path through the wedge pair becomes the ordinary path through the compensation crystal. The waveplate cut ensures that the e-axis lies in the plane perpendicular to the optical path. With length $l_c = 2l_w$ (under that assumption that the wedge and compensation parts are the same material) the DGD is eliminated to first order. Second-order corrections can be made to account for the refracted paths in the crystals.

The differential beam displacement $d_v - d_u$ can also be corrected by cutting the compensation crystal to rhombohedral angle θ_r. In general, the refraction angle into the crystal depends on the input polarization. The e- and o-ray refraction angles in the small-angle approximation are

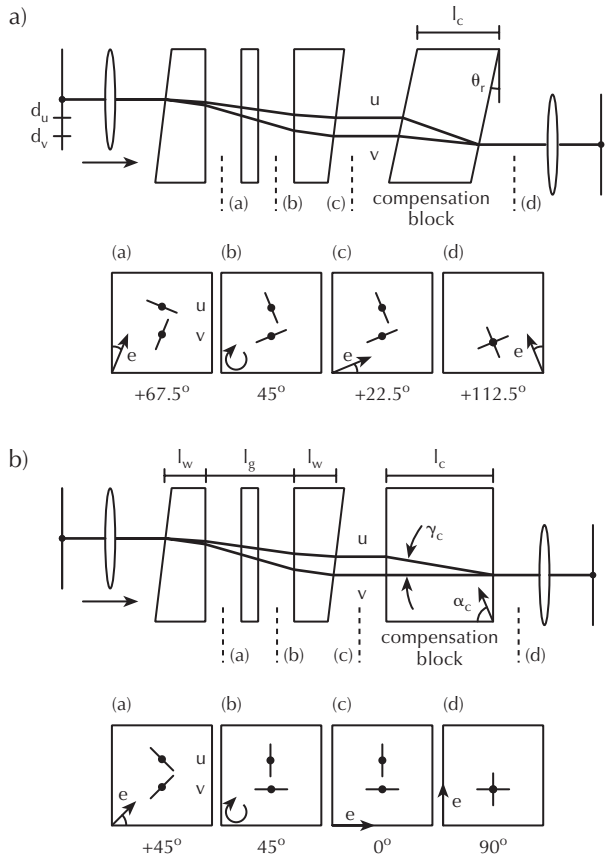


Fig. 6.12. Forward ray-trace diagrams of Swan and Xie PMD-compensated deflection-type isolators. a) Swan method uses compensation crystal cut as a waveplate and rhombohedral angle θ_r to compensate the DGD from the wedge pair and to refract differentially the u- and v-paths. b) Xie method uses compensation crystal cut as a partial walkoff and partial waveplate parallelepiped to compensate the DGD from the wedge pair and to translate the u-path onto the v-path.

$$\theta_{e,o} = \left(\frac{1}{n_{e,o}} - 1\right)\theta_r \tag{6.6.1}$$

The difference in displacement through the compensation crystal is therefore

$$d_e - d_o = l_c\theta_r\left(\frac{1}{n_e} - \frac{1}{n_o}\right) \tag{6.6.2}$$

The differential beam displacement due to the wedge pair, (6.3.4) on page 256, is cancelled by the compensation crystal when the two displacements are equal. The required rhombohedral angle is therefore

$$\theta_r = \frac{d_v - d_u}{l_c\left(\frac{1}{n_e} - \frac{1}{n_o}\right)} \tag{6.6.3}$$

Precisely speaking, a non-zero rhombohedral angle requires the plane in which the extraordinary axis of the compensation crystal lies to be tilted so that the refracted paths remain perpendicular to that plane. This prevents walkoff.

Figure 6.12(b) shows the orientation of the three birefringent crystals in the Xie scheme. There are two mechanisms that simultaneously affect the light through the compensation crystal. One is the walkoff experienced by one path because the e-axis of the crystal is cut with a vector component along the optical path. The other is differential-group delay experienced because one path sees the ordinary index and the other sees an effective index that depends on the inclination angle of the e-axis. The compensation crystal length l_c and e-axis inclination angle α_c are tailored to compensate the DGD and differential beam displacement.

Two equations with two free parameters together determine the length and e-axis angle of the compensation crystal. The DGD of the crystal is

$$\tau_c = \frac{l_c\left(n_{\mathrm{g}}(\alpha_c) - n_{\mathrm{g,o}}\right)}{c} \tag{6.6.4}$$

and the differential beam displacement is

$$d_v - d_u = l_c \tan\gamma_c(\alpha_c) \tag{6.6.5}$$

The effective index $n_{\mathrm{eff}}(\alpha_c)$ is given by (3.6.26) on page 117, or for normal incidence,

$$n_{\mathrm{eff}} = \frac{n_e n_o}{\sqrt{n_e^2\cos^2(\alpha_c) + n_o^2\sin^2(\alpha_c)}} \tag{6.6.6}$$

The walkoff angle, (3.6.15) on page 110, is also governed by the inclination angle:

$$\tan\gamma_c = \frac{\left(n_e^2 - n_o^2\right)\sin\alpha_c\cos\alpha_c}{n_e^2\cos^2\alpha_c + n_o^2\sin^2\alpha_c} \tag{6.6.7}$$

As a technical point, the group indices are used in (6.6.6) while the refractive indices are used in (6.6.7). The two free parameters in these two equations are l_c and α_c. Given the DGD from the wedge pair and the displacement $d_v - d_u$, a unique solution can be found.

Note that a shortcoming of the Xie design is that the e-axis orientation in the two wedges is different than before (Figure 6.12(b)). To recombine the u- and v-paths perfectly, the linear polarization state orientation should be parallel and perpendicular to the walkoff direction.

Table 6.1 shows the improvement of a single-stage deflection-type PMD-compensated isolator over single-stage deflection-type isolator. It is not known which of the two compensation schemes is used for this product.

Displacement-type isolators can also have PMD-compensation. The best overall performance with the fewest parts is a two-stage configuration similar to the original Chang and Sorin proposal [3] but with a variation proposed by Konno [10] and further improved here. Using the spot-vector diagrams so clearly presented in [11], four displacement-type isolators and their behavior are illustrated in Fig. 6.13. Another variation of the spot diagram is found in [14], and an alternative PMD-compensation scheme for displacement-type isolators is reported in [27].

The original Chang and Sorin device [2] is shown in Fig. 6.13(a). The associated spot-vector diagrams trace the beam locations through the device in a plane perpendicular to the optical path. In the forward direction, both input polarizations begin at point P_o. The first and second walkoff blocks translate the v-path along vectors p_{v1} and p_{v2}, respectively. The third block translates the u-path along vector p_u to combine the two beams. In the reverse direction, the input polarizations begin at point P_o' and trace the indicated paths. Both beams are displaced out of the P_o aperture, leading to isolation.

The path lengths p_u and p_v are analogues for the DGD accrued through the isolator core. The optical phase of either path through a crystal is $\phi = \omega nL/c$. The phase difference between a walkoff path and the associated straight-through path is $\Delta\phi = \omega(n_{\text{eff}} - n_o)L/c$, or, accounting for the walkoff angle γ,

$$\Delta\phi = \frac{\omega}{c}(n_{\text{eff}} - n_o)p_{u,v}\cot\gamma \tag{6.6.8}$$

Provided that the e-axis inclination angle is the same for each crystal, ensuring that n_{eff} and γ are constant, the path-length difference $p_v - p_u$ is proportional to the DGD. The first Chang and Sorin isolator has a DGD that goes as $\tau \propto \sqrt{2}a$, where a is the unit crystal length.

Clearly, then, the two-stage Chang and Sorin component [3] (Fig. 6.13(b)) has a DGD that scales as $\tau \propto (2 - \sqrt{2})a$. Recognizing the importance of path balancing, Kuzuta proposes the modified two-stage block isolator shown in Fig. 6.13(c). Addition of the second $\sqrt{2}a$-length block translates both u- and v-paths equally. As shown in the diagram, $p_{u1} + p_{u2} = p_{v1} + p_{v2}$.

A more economic and elegant approach is shown in Fig. 6.13(d), which is a variation of the Konno proposal [10]. The path lengths are balanced by increasing the effective index of the p_u in relation to the v-paths. Using (6.6.8) and $\tau = d\Delta\phi/d\omega$, the path lengths are balanced when

$$(n_{\text{g-eff}}(\alpha_c) - n_{\text{g,o}})\cot\gamma_c = \sqrt{2}\,(n_{\text{g-eff}} - n_{\text{g,o}})\cot\gamma \tag{6.6.9}$$

The center crystal has to be lengthened accordingly. This scheme is a small change to the original Chang and Sorin two-stage proposal but with the significant improvement in DGD mitigation.

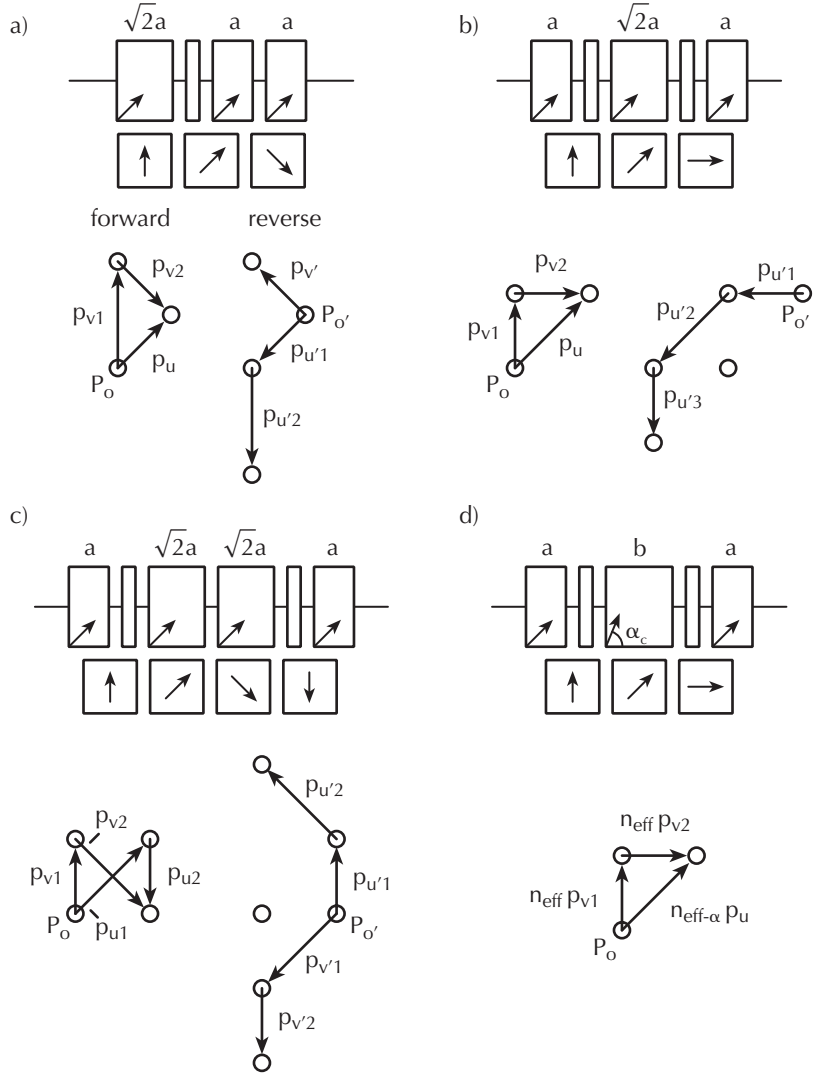


Fig. 6.13. Displacement isolators, non-PMD-compensated (a,b) and PMD-compensated (c,d), with corresponding spot vector diagrams. a) Single-stage displacement isolator as before. Forward path lengths are such that $p_{v1} + p_{v2} \neq p_u$, generating PMD. b) Dual-stage displacement isolator as before. c) PMD-compensated dual-stage displacement isolator. Forward path lengths are equalized between the two polarizations. d) Elegant PMD-compensated dual-stage displacement isolator. Orientation of extraordinary axis in second block increases the u-path delay to equalize to the v-path.

References

1. D. W. Anthon and D. L. Sipes, "Multi-function optical isolator," U.S. Patent 6,088,153, July 11, 2000.
2. K. W. Chang and W. V. Sorin, "Polarization independent isolator using spatial walkoff polarizers," *IEEE Photonics Technology Letters*, vol. 1, no. 3, pp. 68–80, 1989.
3. ——, "High-performance single-mode fiber polarization-independent isolators," *Optics Letters*, vol. 15, no. 8, pp. 449–451, 1990.
4. Y. Cheng and G. S. Duck, "Multi-stage optical isolator," U.S. Patent 5,768,005, June 16, 1998.
5. D. J. Gauthier, P. Narum, and R. W. Boyd, "Simple, compact, high-performance permanent-magnet faraday isolator," *Optics Letters*, vol. 11, no. 10, pp. 623–625, 1986.
6. A. J. Heiney and D. K. Wilson, "Optical isolators employing oppositely signed faraday rotating materials," U.S. Patent 5,087,984, Feb. 11, 1992.
7. Y. Huang, P. Xie, X. Luo, and L. Du, "Optical isolator with reduced insertion loss and minimized polarization mode dispersion," U.S. Patent 2002/0 060 843, May 23, 2002.
8. R. S. Jameson, "Polarization independent optical isolator," U.S. Patent 5,033,830, July 23, 1991.
9. "Micro optics for telecom catalog 2002," Kocent Communications, Fuzhou, Fujian, P.R. China, 2002. [Online]. Available: http://www.koncent.com/
10. Y. Konno, S. Aoki, and K. Ikegai, "Polarization independent optical isolator," U.S. Patent 5,774,264, June 30, 1998.
11. N. Kuzuta, "Optical isolator," U.S. Patent 5,237,445, Aug. 17, 1993.
12. T. Matsumoto, "Polarization-inpdependent isolators for fiber optics," *Electronics and Communicatinos in Japan*, vol. 62-C, no. 7, pp. 113–119, 1979.
13. ——, "Optical nonreciprocal device," U.S. Patent 4,239,329, Dec. 16, 1980.
14. H. Ohta and N. Nakamura, "Optical isolator," U.S. Patent 5,151,955, Sept. 29, 1992.
15. J.-J. Pan, "Highly miniatured, folded reflection optical isolator," U.S. Patent 6,212,305, Apr. 3, 2001.
16. F. J. Sansalone, "Compact optical isolator," *Applied Optics*, vol. 10, no. 10, pp. 2329–2331, 1971.
17. K. Shirai, M. Sumitani, N. Takeda, and M. Arii, "Optical isolator," U.S. Patent 5,278,853, Jan. 11, 1994.
18. K. Shiraishi, F. Tajima, and S. Kawakami, "Compact faraday rotator for an optical isolator using magnets arranged with alternating polarities," *Optics Letters*, vol. 11, no. 2, pp. 82–84, 1986.
19. K. Shiraishi and S. Kawakami, "Cascaded optical isolater configuration having high-isolation characteristics over a wide temperature and wavelength range," *Optics Letters*, vol. 12, no. 7, pp. 462–464, 1987.
20. K. Shiraishi, S. Sugaya, and S. Kawakami, "Fiber faraday rotator," *Applied Optics*, vol. 23, no. 7, pp. 1103–1105, 1984.
21. M. Shirasaki, "Optical device," U.S. Patent 4,548,478, Oct. 22, 1985.
22. M. Shirasaki and K. Asama, "Compact optical islator for fibers using birefringent wedges," *Applied Optics*, vol. 21, no. 23, pp. 4296–4299, 1982.
23. J. Y. Song, "Optical isolator," U.S. Patent 6,061,167, May 9, 2000.

24. C. B. Swan, "Optical isolator with polarization dispersion and differential transverse deflection correction," U.S. Patent 5,631,771, May 20, 1997.
25. ——, "Optical isolator with polarization dispersion and differential transverse deflection correction," U.S. Patent 5,930,038, July 27, 1999.
26. T. Uchida and A. Ueki, "Optical isolator," U.S. Patent 4,178,073, Dec. 11, 1979.
27. T. Watanabe, S. Sugiuama, and T. Ryuo, "Multiple-stage optical isolator," U.S. Patent 6,049,425, Apr. 11, 2000.
28. C. G. Young, "Multiple wavelength optical isolator," U.S. Patent 3,602,575, Aug. 31, 1971.